

Parametric resonance of capillary waves at the interface between two immiscible Bose-Einstein condensates

D. Kobayakov,¹ V. Bychkov,¹ E. Lundh,¹ A. Bezett,² and M. Marklund¹

¹*Department of Physics, Umeå University, 901 87 Umeå, Sweden*

²*Institute for Theoretical Physics, Utrecht University, Leuwanlaan 4, 3584 CE Utrecht, The Netherlands*

(Received 15 June 2012; published 13 August 2012)

We study the parametric resonance of capillary waves on the interface between two immiscible Bose-Einstein condensates pushed towards each other by an oscillating force. Guided by analytical models, we solve numerically the coupled Gross-Pitaevskii equations for a two-component Bose-Einstein condensate at zero temperature. We show that, at moderate amplitudes of the driving force, the instability is stabilized due to nonlinear modifications of the oscillation frequency. When the amplitude of the driving force is large enough, we observe a detachment of droplets from the Bose-Einstein condensates, resulting in the generation of quantum vortices (skyrmions). We analytically investigate the vortex dynamics, and conditions of quantized vortex generation.

DOI: [10.1103/PhysRevA.86.023614](https://doi.org/10.1103/PhysRevA.86.023614)

PACS number(s): 03.75.Mn, 03.75.Kk, 47.20.Ma

I. INTRODUCTION

Numerous recent studies of hydrodynamic phenomena in quantum media have demonstrated remarkable interplay between quasiclassical hydrodynamics and purely quantum effects such as quantum solitons and vortices (e.g., see Refs. [1–6]). As an example of such interplay, we can mention works on shock fronts in Bose-Einstein condensates (BECs), nonlinear optics, and quantum plasmas [7–9]: the quantum shocks propagate as soliton trains due to Bohm–de Broglie dispersion instead of the monotonic transition between low-density and high-density gases (fluids, plasmas) in a classical shock. Development of quantum solitons has been also obtained experimentally and theoretically in the process of dynamical quantum interpenetration of both miscible and immiscible BECs [2,10,11].

Another important example of the interplay concerns the generation of quantized vortices. Traditionally, quantum vortices in BECs are produced by rotating the trap [12], by stirring BECs by moving potentials [13], by coherent transfer of the orbital angular momentum of photons to atoms [14], by adiabatic phase imprinting [15], or by the modulational instability of solitons [16,17]. Recently, there has been also much interest in multicomponent BECs with a well-distinguished interface, which allow the possibility of vortex generation by means of quasiclassical hydrodynamic instabilities: the Kelvin-Helmholtz instability, the Rayleigh-Taylor (RT) instability, the capillary instability, etc. [4–6,18–21]. With the help of the instabilities, one can produce rather complicated quantum vortex structures in BECs like skyrmions, for which the intrinsically empty vortex core in one BEC component is filled by the other component [11,21]. The system of a two-component BEC can be realized experimentally by blocking the spin-recombination process $|1, -1\rangle + |1, 1\rangle \rightarrow |1, 0\rangle + |1, 0\rangle$ by the quadratic Zeeman effect, as discussed in Ref. [18]. In the case of a magnetic gradient pushing the BEC components towards each other, they tend to reduce the potential energy of the system by exchanging places, which typically happens in the form of a multidimensional flow due to the RT instability. In that sense, the magnetic field gradient plays a role similar to a gravitational field for the classical RT instability. As an alternative to the RT instability, Ref. [11]

found the possibility of reducing the excess of potential energy by one-dimensional (1D) dynamical quantum interpenetration; still, it has been also shown that the RT instability dominates for interface perturbations of a sufficiently large wavelength.

Linear stability analysis based on the variational principle [20] has demonstrated that the same experimental configuration may also reproduce other quasihydrodynamic phenomena in BECs such as the Richtmyer-Meshkov instability and the parametric instability by using a time-dependent magnetic field, which corresponds to time-dependent effective “gravity.” We focus on the parametric resonance, which is also known as the parametric or Faraday instability. We point out that interface dynamics driven by time-dependent gravity is intensively studied within the classical fluid (gas) mechanics; e.g., see recent numerical simulations of the Richtmyer-Meshkov instability in gases [22–24], laboratory experiments on fluids with oscillating effective “gravity” [25,26], and works on inertial confined fusion [27,28] and combustion [29–32]. In classical hydrodynamics, the parametric instability is typically excited at the interface between light and heavy gases (fluids) with the “gravity” produced by direct vibrations of the experimental setup or by acoustic waves (the latter is especially typical for combustion systems). In particular, experimental and numerical studies of the parametric instability in combustion encountered powerful turbulence produced in the flow because of the instability [29,33,34].

In the present paper we study the development of the parametric instability at the interface of two immiscible BEC components pushed towards each other by an oscillating force. The instability arises due to the parametric resonance pumping quantum capillary waves at the interface. We show that in the present configuration the instability does not lead to turbulence. At moderate amplitudes of the driving force the instability is stabilized at the nonlinear stage due to modifications of the doubled oscillation frequency in comparison with the frequency of the driving force. When the amplitude of the driving force is large enough, we observe a detachment of droplets from BEC components and the generation of quantum vortices (skyrmions). We discuss the properties and dynamics of the skyrmions.

II. ANALYTICAL MODEL FOR THE PARAMETRIC RESONANCE

Two immiscible BECs are separated in space in the ground state of the system. To investigate the physics of the dynamical system it is sufficient to study a symmetric case, where the components' atoms have equal masses, and equal intracomponent interaction parameters $g \equiv g_{11} = g_{22}$, $g_{12} > g$, where $g_{ij} \equiv 4\pi\hbar^2 a_{ij}/m$ and a_{ij} are the scattering lengths for collisions between atoms of the i th and j th components. The scattering lengths are calculated depending on the geometry of the system confinement [35]; the dimensionless parameter $\gamma \equiv g_{12}/g - 1 > 0$ specifies the strength of mutual repulsion of the components. We study a ribbon-shaped two-dimensional (2D) geometry where the BEC components are initially placed in the domains $y < 0$ and $y > 0$, respectively. The BEC is tightly confined in the z direction; in the y direction it is trapped so that the Thomas-Fermi (TF) approximation for each component holds well [11]; finally, it is not confined in the x direction. The system of width $\tilde{\lambda}$ along the x direction is shown in Fig. 1, with periodic boundary conditions imposed along the x axis. Within the analytical models the ribbon may be treated as initially uniform in the y direction with negligible influence of the trap edges. Still, a finite length of the ribbon is required in the numerical solution to the Gross-Pitaevskii (GP) equations.

In the case of zero external forcing, linear stability analysis [36] predicts a perturbation mode, which may be interpreted as quantum capillary waves with the frequency $\tilde{\Omega}_c$ depending on the wave number $\tilde{k} = 2\pi/\tilde{\lambda}$ as

$$\tilde{\Omega}_c^2 = \tilde{k}^3 \frac{\hbar^2 \tilde{n}_0^{1/2}}{2m^2} \sqrt{2\pi (a_{12} - a)}, \quad (1)$$

where a tilde indicates dimensional values and \tilde{n}_0 is the condensate density at the unperturbed infinitely thin interface (i.e., in the Thomas-Fermi approximation). Taking into account a time-dependent magnetic force pushing BECs towards each other, we obtain an equation for the linear interface perturbations [20],

$$\left[\frac{d^2}{d\tilde{t}^2} + \tilde{\Omega}_c^2 - \tilde{k} \frac{\mu_B B'(\tilde{t})}{2m} \right] \tilde{\zeta}(\tilde{t}) = 0, \quad (2)$$

where $\tilde{\zeta}(\tilde{t})$ is the amplitude of deviation of the interface from hydrostatic equilibrium, μ_B is the Bohr magneton, and $B'(\tilde{t})$ indicates the external (Stern-Gerlach) force due to the magnetic field gradient.

We consider a harmonically oscillating force, which may lead to the parametric instability. For simplicity of design,

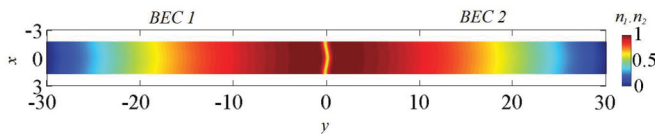


FIG. 1. (Color online) The system geometry: density distribution for two immiscible BECs, n_1 and n_2 , for $R_0 = 30$, with initial perturbations at the interface. The BECs are tightly trapped in the z direction (which means quasi-2D geometry), trapped with resulting TF profile in the y direction, and uniform in the x direction. Dimensionless units are defined in Sec. II.

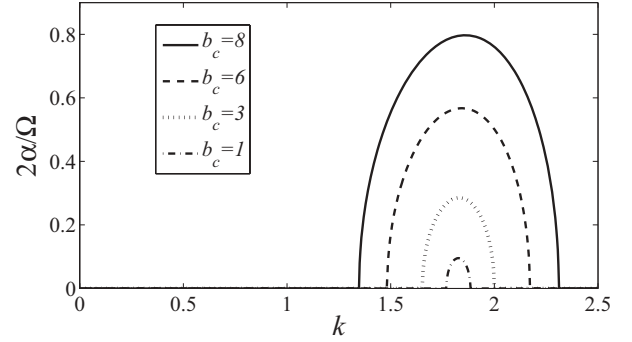


FIG. 2. Scaled growth rate of the parametric instability vs the wave number of the interface perturbation between BECs for $\Omega = 8.55$ and different amplitudes of the driving force, obtained in Ref. [20]. Dimensionless units are defined in Sec. II.

nations, we use the standard scalings for a trapped system with the length scales measured in units of the oscillator characteristic length $a_y = \sqrt{\hbar/m\omega_y}$, time in units of $(2\omega_y)^{-1}$, and wave functions in units of $\sqrt{\tilde{n}_0}$. Within these designations, the dimensionless system size is $R_0 = \sqrt{2g\tilde{n}_0/\hbar\omega_y}$ and the dispersion relation for the capillary waves is $\Omega_c^2 = \sqrt{\gamma} R_0 k^3$. In the same manner we define the dimensionless external force $b(t) = \mu_B B'(t)a_y/\hbar\omega_y$, which we take in the form

$$b(t) = b_c \sin(\Omega t). \quad (3)$$

The approximate analytical solution to Eq. (2) with the oscillating force may be obtained using the method of Ref. [37], which describes exponential growth of interface perturbations as

$$\zeta = \zeta_0 \sin(\Omega t/2 + \varphi) \exp(\alpha t) \quad (4)$$

with the growth rate α , some amplitude ζ_0 , and the phase shift φ with respect to the driving force. Mark that the growth of the parametric instability is accompanied by interface oscillations with frequency $\Omega/2$. Then the perturbation growth rate may be found analytically using the equation

$$\left(\alpha^2 - \frac{\Omega^2}{4} + \Omega_c^2 \right)^2 - \frac{b_c^2 k^2}{4} + \alpha^2 \Omega^2 = 0 \quad (5)$$

(see Ref. [20] for details); the growth rate is plotted vs the perturbation wave number in Fig. 2 for $\Omega = 8.55$ and different amplitudes of the driving force. As we can see, maximal growth rate is achieved for the frequency of the driving force equal to double the capillary frequency, $\Omega = 2\Omega_c$, which is the condition of a parametric resonance. In that case the growth rate is given by a simple formula,

$$\alpha^2 = \sqrt{4\Omega_c^4 + b_c^2 k^2} - 2\Omega_c^2, \quad (6)$$

and the parametric instability may be excited even by an extremely weak force. For other frequencies of the driving force, out of the resonance $\Omega \neq 2\Omega_c$, a finite force amplitude b_c is required to produce the instability.

We point out that in the case of moderate amplitude of the driving force, the instability domain in wave numbers is strongly localized around the resonance point (see Fig. 2). Another interesting characteristic of the linear stage is the relative value of the instability growth rate α and the perturbation frequency $\Omega/2$ in Eq. (4), which shows how

fast the perturbations grow in one oscillation period of the driving force. As we see below, the instability parameter $2\alpha/\Omega$ determines the strength of the process and the qualitative regime of the parametric resonance at the nonlinear stage.

Let us qualitatively discuss the dynamics of the interface expected at the nonlinear stage of the parametric resonance, for the cases of weak instability ($2\alpha/\Omega \ll 1$) and strong instability ($2\alpha/\Omega \gg 1$). The transition between these two regimes happens for $2\alpha/\Omega \sim 1$. In the case of weak instability one should expect nonlinear stabilization of the parametric resonance because of nonlinear modifications of the oscillation frequency [37]. Taking into account the small but finite amplitude of the oscillations ζ_0 , one finds the oscillation frequency modified from $\Omega/2$ to $\Omega/2 - \kappa\zeta_0^2$, where κ is some factor, which may be found, e.g., from the numerical solution. Since the frequency changes together with the growth of the perturbation amplitude, the system eventually leaves the instability domain and the perturbation growth is saturated. Substituting the modified frequency into Eq. (5) and taking $\alpha = 0$ we evaluate the maximal oscillation amplitude attained in the resonance as

$$\zeta_0 = \sqrt{b_c k / 2\Omega\kappa}. \quad (7)$$

In the opposite limit of strong instability, $2\alpha/\Omega \gg 1$, the approach of small corrections to the linear solution employed in Ref. [37] fails. In that case we expect considerable growth of the perturbation amplitude already on one oscillation period with strongly nonlinear effects resembling qualitatively the RT instability, though with time-dependent effective gravity.

III. NUMERICAL SOLUTION

We investigate the parametric resonance numerically by solving the coupled Gross-Pitaevskii equations

$$i\hbar \frac{\partial}{\partial t} \tilde{\psi}_1 = \left[-\frac{\hbar^2}{2m} \Delta_{x,y} + \tilde{V}_1 + g_{11} |\tilde{\psi}_1|^2 + g_{12} |\tilde{\psi}_2|^2 \right] \tilde{\psi}_1, \quad (8)$$

$$i\hbar \frac{\partial}{\partial t} \tilde{\psi}_2 = \left[-\frac{\hbar^2}{2m} \Delta_{x,y} + \tilde{V}_2 + g_{22} |\tilde{\psi}_2|^2 + g_{12} |\tilde{\psi}_1|^2 \right] \tilde{\psi}_2, \quad (9)$$

where $\Delta_{x,y} \equiv \partial_{xx}^2 + \partial_{yy}^2$, and the potentials $\tilde{V}_{1,2}(t,x,y)$ include both the trapping potential and the driving potential as $\tilde{V}_j \equiv m\omega^2(x^2 + y^2)/2 + (-1)^j \mu_B B'(t)y/2 \equiv \tilde{V}_t + (-1)^j \tilde{V}_d$. The trapping potential along the z axis is supposed to be much stronger than the two-particle interaction energy, and this leads to renormalization of the interaction parameters [35]. In all calculations, we keep the scaled system size $R_0 = 30$ and the repulsion parameter $\gamma = 0.01$, which implies a sufficiently small thickness of the interface $\sim 1/\sqrt{\gamma}R_0 \approx 0.3$ and a much smaller healing length $\sim 1/R_0 \approx 3.3 \times 10^{-2}$ [11]. The unperturbed planar distribution of BEC density has been obtained numerically similar to Refs. [11,19].

At $t = 0$ we impose a cosine-shaped perturbation at the interface as shown in Fig. 1, which corresponds to the capillary mode with the perturbation wavelength $\lambda = 3.44$, and immediately turn on the driving magnetic (Stern-Gerlach) force and study the dynamics of the system for different amplitudes of

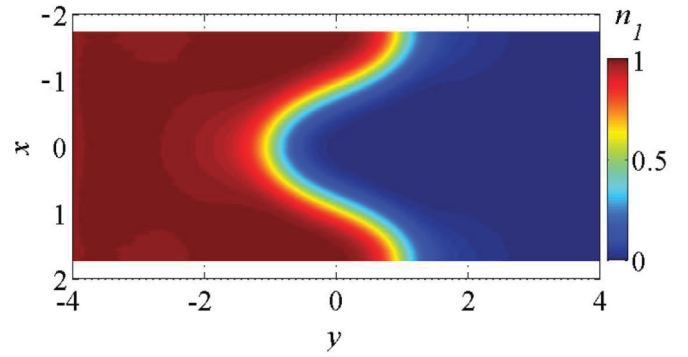


FIG. 3. (Color online) Density distribution of BEC 1, n_1 , for $R_0 = 30$, $b_c = 3$ at $t = 2.0$, showing the maximal interface deformation in the regime of nonlinearly stabilized parametric resonance. Dimensionless units are defined in Sec. II.

the force $b_c = 1-10$. Since we are interested in the parametric resonance, then we choose the external force frequency $\Omega = 8.55$ equal to $2\Omega_c$ as calculated for the wavelength $\lambda = 3.44$ of the initial perturbations. In order to define the position of the interface in the study, we choose the density level equal to the density of the unperturbed solution at $z = 0$.

The system dynamics at the nonlinear stage of the resonance depends qualitatively on the magnitude of the external force b_c . In the case of relatively weak force, e.g., for $b_c = 1,3$, the shape of the interface resembles the initial cosine-shaped perturbations, though with increased amplitude. As an example, maximal distortion of the interface for $b_c = 3$ is demonstrated in Fig. 3 for the time instant $t = 2.0$. The time dependence of the perturbation amplitude for $b_c = 1,3$ may be characterized as rather regularly modulated oscillations (see Fig. 4), with frequency $\approx \Omega/2$ and with the maximal interface distortion attained after three or four oscillations. After that, the dynamics of the interface deviation amplitude is reproduced periodically in the form of modulations. We point out that the force magnitudes $b_c = 1,3$ belong to the limit of weak instability with the instability parameter $2\alpha/\Omega = 0.095, 0.29$, respectively. Thus, in agreement with the expectations of the analytical model, the parametric resonance is stabilized at the nonlinear stage in the case of weak instability. Numerical simulations indicate that the

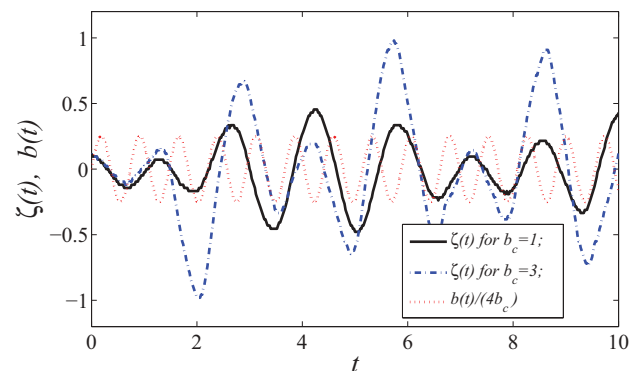


FIG. 4. (Color online) Amplitude $\zeta(t)$ of the interface deviation from equilibrium for $R_0 = 30$ and $b_c = 1,3$ and the scaled amplitude of the driving force (dots). Dimensionless units are defined in Sec. II.

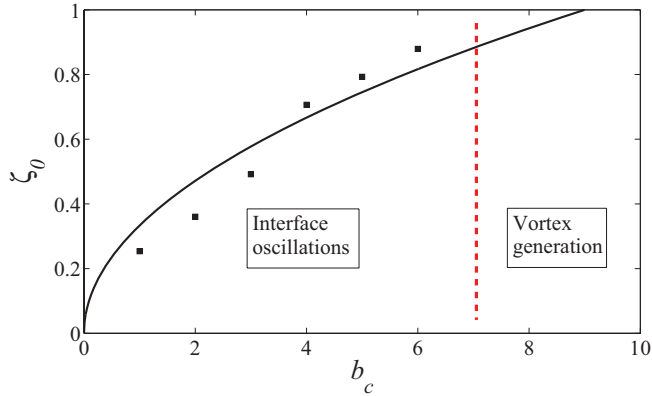


FIG. 5. (Color online) Phase diagram of vortex generation in the fixed-size (fixed R_0) system, showing possible regimes with well-defined interface. For $b_c \geq 10$ the system is not well described in the mean-field approximation because it acquires too many incoherent excitations. The mean deviation of the interface from equilibrium ζ_0 , averaged over twice as many periods of modulations, as shown in Fig. 4, for various b_c (time averaged for irregular dependence), $R_0 = 30$. The solid line corresponds to the analytical model (7) with $\kappa = 0.96$. The dashed line separates two qualitatively different nonlinear regimes. Dimensionless units are defined in Sec. II.

oscillation amplitude increases with increasing magnitude of the driving force as shown in Fig. 5: comparison of the numerical results with Eq. (7) demonstrates good agreement and allows evaluating the factor κ for the chosen problem parameters as $\kappa = 0.96$.

Taking a larger force magnitude, $b_c = 6$, we obtain the instability parameter comparable to unity, $2\alpha/\Omega = 0.57$, which leads to considerable nonlinear effects in the interface dynamics presented in Fig. 6 for selected time instants $t = 0.08$ – 3.46 . Starting with a small initial perturbation, the interface oscillates with noticeably smaller frequency than $\Omega/2$. In addition, the oscillations are accompanied by strong broadening of the interface on the reversal motion of humps transformed into hollows, e.g., at $t = 1.14$. The second growth of the hump on the snapshots $t = 1.66$ – 2.08 is characterized by the complicated shape of the interface, quite distinct from the original harmonic perturbation. We note the resemblance of the interface shape at $t = 2.08$ and the “mushroom” structures for the RT instability [18,20]. Due to the large amplitudes, we observe the tendency of the mushroom cap to detach from the main bulk of the BEC at $t = 2.4$ and to form a large blob, i.e., a 2D soliton, according to the mechanism discussed in Ref. [19]. The mechanism of the blob detachment is also related to the capillary instability studied in Ref. [21]. Collapse of the mushroom structure may be also compared to the parametric resonance observed in the combustion system of a flame front in the effective gravitational field produced by sound [33,34]. Still, in the case of $b_c = 6$, detachment of the blob is not complete, and it is followed by reattachment at $t = 2.66$. Because of the detachment-reattachment process, the definition of the oscillation amplitude becomes ambiguous, which leads, in particular, to irregularities in the plot of $\zeta(t)$. Reattachment of the blob to the bulk of the BEC is accompanied by momentum transfer, i.e., bounce, which produces a grey soliton traveling in the bulk of the BEC to the left in the snapshot at $t = 3.46$.

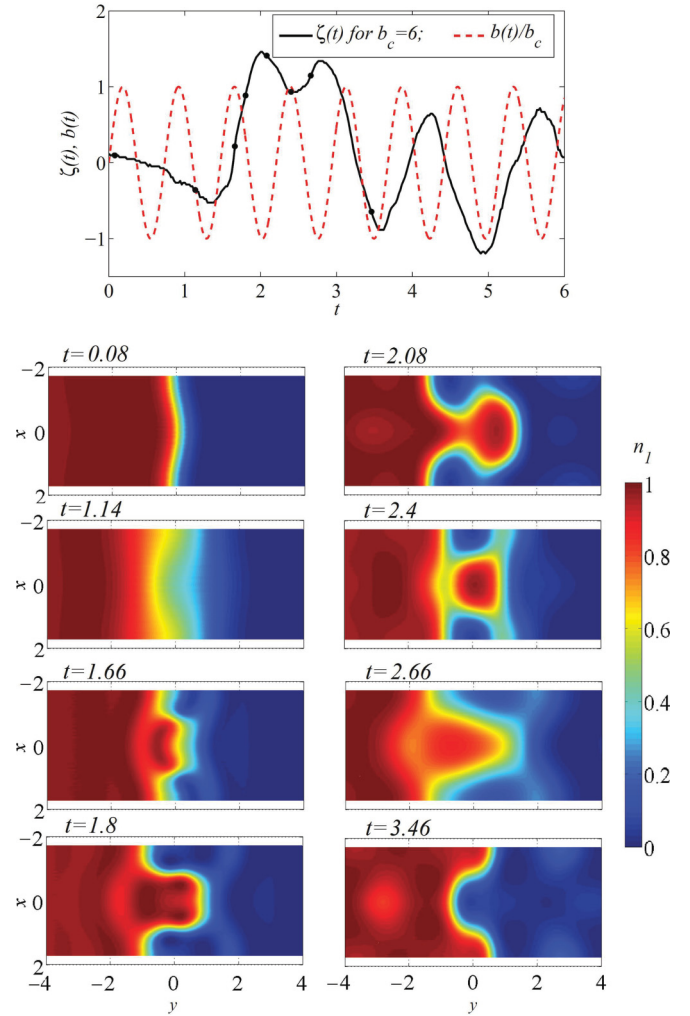


FIG. 6. (Color online) Top: The scaled amplitude of the driving force, and amplitude of the interface deviation from equilibrium for $R_0 = 30$ and $b_c = 6$; the markers indicate the time instants for the density snapshots (bottom). Bottom: Snapshots of density distribution of BEC 1, n_I . Dimensionless units are defined in Sec. II.

The soliton is formed because the mean squared deviation of the external force is well above the critical value $b_{cr} = \gamma R_0/2$ discussed in detail in Ref. [11]. At the same time, the interface dynamics for $b_c = 6$ does not lead to production of vortices, and most of the effects, except the production of grey solitons, may be described within the quasiclassical approach.

Generation of vortices may be observed at a larger magnitude of the driving force, $b_c = 8$ – 10 in our simulations. The approximate boundary between two regimes is indicated in Fig. 5 by the dashed vertical line, and it corresponds to the instability parameter about $2\alpha/\Omega = 0.8$, i.e., close to unity, in agreement with the expectation of the analytical model. Figure 7 presents the amplitude of the interface deviation from equilibrium for $b_c = 8$ – 10 until the instants of droplet detachment and formation of quantum vortices in BEC 1 with the vortex core filled by BEC 2 and vice versa—skyrmions. After that instant, the definition of the interface deviation becomes ambiguous. As we can see in Fig. 7, skyrmions are generated after several interface oscillations for $b_c = 8, 9$, and on the very first oscillation for $b_c = 10$. Similar to Fig. 6, the oscillations are

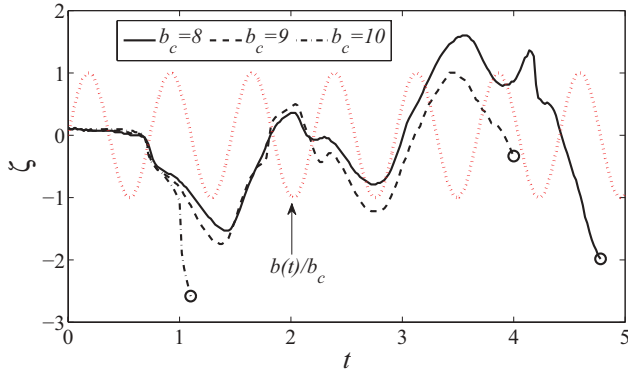


FIG. 7. (Color online) Amplitude of the interface deviation from equilibrium for $R_0 = 30$ and $b_c = 8-10$, and the scaled amplitude of the driving force. The time instants of vortex detachment are indicated by circles. Dimensionless units are defined in Sec. II.

extremely irregular with characteristic frequency noticeably smaller than $\Omega/2$. Taking the simulation run for $b_c = 8$ as an example, we observe the front shape in the oscillations for $t < 4.5$ resembling qualitatively the structures presented in Fig. 6. For this reason, we focus on the snapshots for $b_c = 8$ and $t \geq 4.5$ in Fig. 8 when qualitatively new quantum effects come into play. In particular, Fig. 8 demonstrates density and phase distributions of BEC 1 for the time instants $t = 4.8$, illustrating detachment of the first droplets (2D solitons); $t = 4.94$, when the soliton splits into the vortex-antivortex pair; $t = 5.12$, when the vortex-antivortex pair becomes almost coalescent because of mutual attraction; and $t = 7.7$, when the vortex-antivortex pair becomes separated again and drifts away from the main bulk of BEC 2. In addition, new vortex-antivortex pairs may be observed at $t = 7.7$.

IV. GENERATION OF VORTICES IN THE PARAMETRIC INSTABILITY

A. Pseudospin description of the two-component BEC

The regime of large-amplitude force is characterized by the generation of quantum vortex-antivortex pairs, so that each of the vortices carries circulation, while total circulation is zero. In the three-dimensional (3D) case, similar vortices would be ring-shaped, though the Kelvin waves can also split the vortex lines into smaller pieces. The ground state and the vortex structure in the two-component BEC are determined by the interaction parameters. Since the system in study is characterized by weak repulsion, $\gamma \equiv g_{12}/g - 1 \ll 1$, the topological excitations are vortices in one component with the core filled by atoms of another component; such a structure is known as an Anderson-Toulouse (AT) vortex. The dynamic states shown in Figs. 8(c) and 8(e) present clear examples of the AT vortex pairs; Fig. 9 shows a cut of BEC densities $n_{1,2}$ taken from Fig. 8(e) at $y = -9.635$, along the line crossing the vortex axes. The obtained vortices may be also described as *skyrmions*, though the term skyrmion refers to a rather wide class of topological solitons. Historically this term originates from the theory by Skyrme [38], which is quite similar mathematically to the description of multicomponent BECs [39]. For a small repulsion parameter $\gamma \ll 1$, the radius of the AT vortex core is given by $\xi_0/\sqrt{\gamma}$, where $\xi_0 = \hbar/\sqrt{2mgn}$,

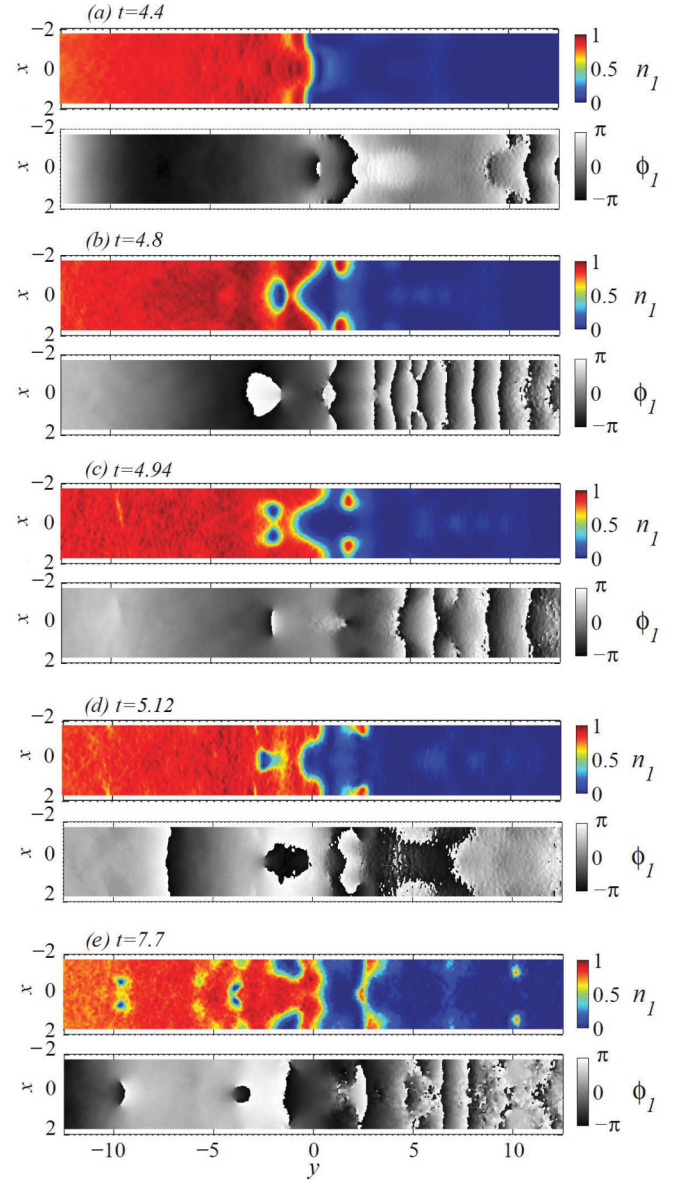


FIG. 8. (Color online) Snapshots of density distribution of BEC 1, n_I , and phase distribution for $R_0 = 30$ and $b_c = 8$, showing vortex generation from the interface between BECs. (b) The detached droplet splits into (c) a vortex-antivortex pair, and this happens periodically (d,e) and further, due to periodic external force. Phase plots show topological excitations. Dimensionless units are defined in Sec. II.

i.e., it is $1/\sqrt{\gamma}$ times larger than the core radius in a single-component BEC. This value is consistent with the vortex structure in Fig. 9, and it is also comparable to the effective width of the interface between the components [20].

Let us describe the generation of vorticity in our system. A natural way to reveal the dynamical difference between single-component and multicomponent BECs is to go over from the representation of the GP Lagrangian and the wave functions (ψ_1, ψ_2) to the representation of a normalized spinor

$$\mathbf{s} = [\chi_1 \exp(i\beta/2), \chi_2 \exp(-i\beta/2)], \quad (10)$$

and the variables $\sqrt{\rho_T} \exp(i\alpha)$ correspond to total density ρ_T and total phase α . The normalization implies $\chi_1^2 + \chi_2^2 = 1$,

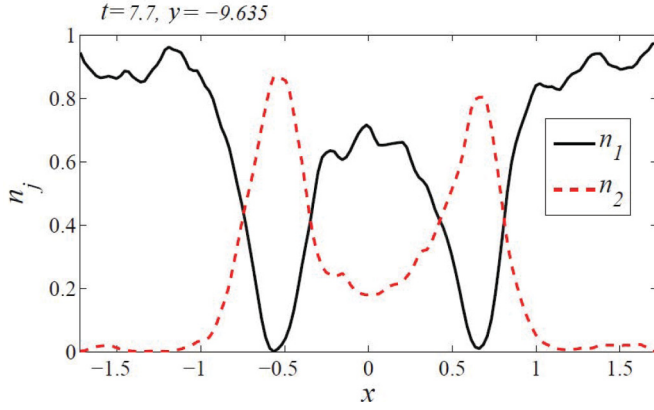


FIG. 9. (Color online) Cut of n_1 and n_2 showing dynamic AT-vortex and antivortex of component 1 (a 2D skyrmion pair) in Fig. 8(d) at $t = 7.7$ and $z = -9.635$. Component 2 fills the vortex cores of component 1. Dimensionless units are defined in Sec. II.

and therefore we can choose $\chi_1 = \cos(\chi/2)$, $\chi_2 = \sin(\chi/2)$; the new variables ρ_T , α , β , and χ are real-valued functions of coordinates and time. If the wave functions are presented as $\psi_j = \sqrt{n_j} \exp(i\phi_j)$, then $\rho_T = n_1 + n_2$, $\alpha = (\phi_1 + \phi_2)/2$, $\beta = \phi_1 - \phi_2$, and $\chi = 2 \arctan \sqrt{n_2/n_1}$.

It is also convenient to define the pseudospin vector as $\mathbf{S} = \bar{\sigma} \sigma$, where $\sigma = (\sigma_x \sigma_y \sigma_z)^T$, and $\sigma_{x,y,z}$ are the Pauli matrices. Then one readily obtains $S_x = \cos \beta \sin \chi$, $S_y = \sin \beta \sin \chi$, and $S_z = \cos \chi$, with the relation $S_x^2 + S_y^2 + S_z^2 = 1$. The superfluid mass current $\rho_T \mathbf{v}_{\text{eff}}$ is derived from equations of motion, Eqs. (8) and (9), as

$$\begin{aligned} \rho_T \mathbf{v}_{\text{eff}} &\equiv |\psi_1|^2 \nabla \arg(\psi_1) + |\psi_2|^2 \nabla \arg(\psi_2) \\ &= \rho_T \left[\nabla \alpha + \frac{\nabla \beta}{2} \cos \chi \right] \\ &= \rho_T \left[\nabla \alpha + S_z \frac{S_y \nabla S_x - S_x \nabla S_y}{2(S_x^2 + S_y^2)} \right]; \end{aligned} \quad (11)$$

see Ref. [40] for derivation of the last term. Equation (11) demonstrates that vorticity $\nabla \times \mathbf{v}_{\text{eff}}$ of the effective superfluid velocity can be nonzero in a multicomponent system without singular regions of the order parameter, in contrast to the single-component case. Using Eq. (11) we compute evolution of vorticity in our system, and plot $\nabla \times \mathbf{v}_{\text{eff}}$ in Fig. 10 for the same moments of time and the same parameters as shown in Fig. 8. This function may be also interpreted as the density of the topological charge, and when integrated over space it gives the topological invariant. This invariant, or Pontryagin index, classifies the stationary states of multicomponent BECs; in our system it is formed from the z component of the vorticity pseudovector, which can be derived from Eq. (11) as [41]

$$q(\mathbf{r}) = \frac{1}{8\pi} \epsilon^{ij} \mathbf{S} [\partial_i \mathbf{S} \times \partial_j \mathbf{S}] = \frac{1}{2\pi} (\nabla \times \mathbf{v}_{\text{eff}})_z. \quad (12)$$

In a more general case the proof of Eq. (12) can be obtained by considering the form $\chi_a \chi_b$, where a, b count the spinor degrees of freedom [41]. The topological charge of a single localized AT vortex is $Q = \int d^2 \mathbf{r} q(\mathbf{r}) = 1$.

One observes that vorticity $\nabla \times \mathbf{v}_{\text{eff}}$ is generated on the interface between BECs. In our superfluid system the interface region may behave locally like a rotating solid body during

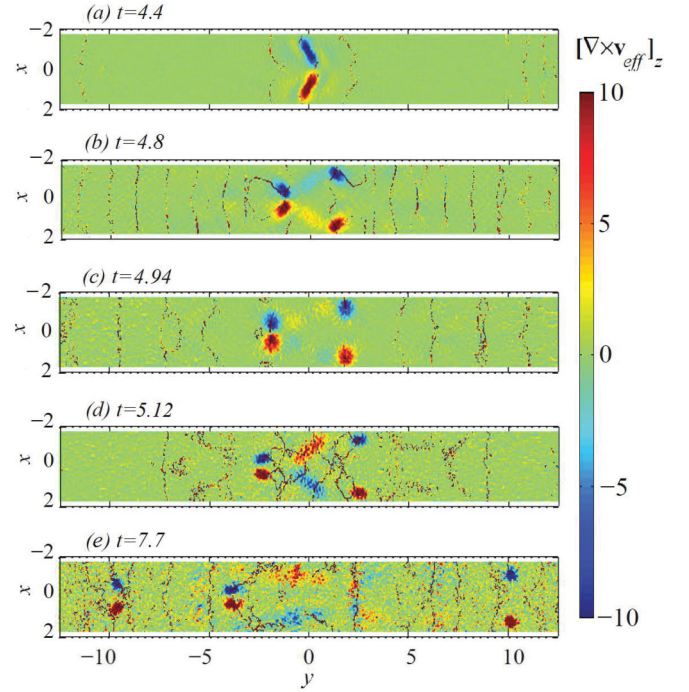


FIG. 10. (Color online) Snapshots of topological charge density of the two-component BEC for $R_0 = 30$ and $b_c = 8$, for time instants the same as in Fig. 8. The topological charge of the system is generated on the interface between BECs. The direction of the z axis is along $\hat{\mathbf{x}} \times \hat{\mathbf{y}}$. Dimensionless units are defined in Sec. II.

some finite time intervals. In particular, such behavior may be observed in Fig. 10(a) for $t = 4.4$, which precedes the detachment of two vortex-antivortex pairs, Fig. 10(b). When the pairs detach, the interface acquires an opposite effective vorticity sign, Fig. 10(c), and then, after a period of capillary oscillations, another vortex-antivortex pair is generated, Fig. 10(d). In Fig. 10 we also observe excitation of compressible modes, which may lead to dissipations due to two-body processes. However, the dissipation processes are beyond the scope of the GP model and are not considered in the present work.

B. Dynamics of vortices

The vortex-antivortex pairs are formed from the bubbles and propagate towards the BEC edge. The pairs are generated on the interface one after another, and they annihilate close to the BEC edge after some sporadic dynamics. In this subsection we investigate the dynamics of the first pair on the stage of propagation towards the edge. In our simulations, interaction between different vortex pairs is negligible, and a typical trajectory of a pair is represented in Fig. 11, where we glue together cuts from the full density profiles taken at ten different time moments. The snapshots are limited by the dashed borders, which show local density.

First let us explain how vortex pairs are formed from the bubbles. Because of the nonlinearity of the process of bubble detachment from the interface it is not clear whether one could predict the initial velocity of the bubble v_0 immediately after the detachment. However, instead we can predict the *critical* velocity of the bubble, above which it splits into vortex pairs. This velocity results from the topology of the order parameter,

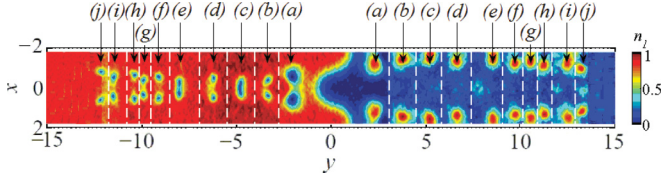


FIG. 11. (Color online) Snapshots of location of the first generated vortex-antivortex pair in component 1 (at $y < 0$), with corresponding fillings of the cores of the first vortex-antivortex pair of component 2 (at $y > 0$), for $R_0 = 30$ and $b_c = 8$. Snapshots are taken at time instants (a) $t = 5.0$, (b) 5.4, (c) 5.8, (d) 6.2, (e) 6.6, (f) 7.0, (g) 7.4, (h) 7.8, (i) 8.2, and (j) 8.6, and only the area close to the pair is shown for each pair (marked by dashed borders). Note that the time instant $t = 5.12$ from Fig. 8(d) is not shown in order to make the picture easier to understand. The second pairs, generated after the first ones, are not shown for the same reason. At the time instant $t = 8.6$, shown in (j), the dynamics of the vortices is sporadic due to localization of the system and strong influence of the external field. Dimensionless units are defined in Sec. II.

because quantized vortices are topological excitations. In the TF approximation, the bubble of BEC 2 produces a cavity in the bulk of BEC 1, which travels with the bubble velocity, and given that the bulk of BEC 1 is at rest, then, up to logarithmic accuracy, its phase must have a “jump” (discontinuity) at the cavity center. This jump can exceed 2π and therefore gives rise to the formation of the vortices, only when diameter L of the bubble exceeds $2\pi\hbar/mv_0$. Therefore, the critical bubble velocity of BEC 2, above which the bubble splits into a vortex-antivortex pair, is

$$v_{\text{cr}} = \frac{2\pi\hbar}{m_1 L}, \quad (13)$$

where m_1 is the mass of the atom of BEC 1 (in our numerical simulations we take $m_1 = m_2 = m$). Equation (13) is valid both for 2D and 3D geometries. We point out that our argument, leading to Eq. (13), is based on the topology of the order parameter and therefore is general. The only assumption made is the validity of the TF approximation $L \gtrsim 2\Delta_{\text{int}}$. The result, Eq. (13), can be applied as well for a single-component BEC when it is stirred by an obstacle with size much larger than the healing length of the BEC. As a result, the number of pairs generated by a bubble with a given initial velocity v_0 is equal to the integer part of v_0/v_{cr} . In our system for $R_0 = 30$, $b_c = 8$, we observe the formation of a single pair from each bubble. We measure the velocity of the first pair as $\approx 1.25\sqrt{\hbar\omega_y/m}$, which is slightly higher than predictions of Eq. (13) computed with $L = 2\Delta_{\text{int}}$ as $v_{\text{cr}} \approx 0.95\sqrt{\hbar\omega_y/m}$. In general one should take into account the compressibility of the bubble [42]; the capillary instability [21] for large bubbles may influence the results too.

Equation (13) can be used to demonstrate that the lowest critical velocity that breaks the Landau criterion of superfluidity is related to topological excitations rather than to soundlike excitations. Indeed, the sound speed c_s in the trap center is equal to $\sqrt{2}R_0$ in the dimensionless variables specified in Sec. II. It should be compared with the dimensionless Eq. (13), $4\pi/L$, where L is the size of the obstacle in units of a_y . Using $L = 2/(\sqrt{\gamma}R_0)$ with $R_0 = 30$, and $\gamma = 0.01$, relevant for droplets seen in the evolution of our system, we obtain

$v_{\text{cr}} \approx 0.44c_s$, and this is confirmed by the observation that the detached droplets split into vortex-antivortex pairs.

Now we turn to the trajectories of the pairs, which are essentially straight lines modulated by relatively weak oscillations. The straight lines indicate the stationary propagation of the pair. Indeed, an isolated stationary vortex pair (vortex ring in three dimensions) moves with a constant velocity with respect to the quiescent bulk when the attraction Magnus force between the vortices in the pair is compensated by the repulsion Magnus force due to the vortex motion. The net Magnus force is equal to zero when the velocity of the vortex pair is the same as the velocity created by one vortex of the pair in the position of the other. The system is invariant with respect to the Galilean coordinate transformation, as can be readily shown in the GP model. However, when the atomic cloud, containing a vortex, is subjected to acceleration, the vortex exhibits inertia due to the mass of the core filling,

$$m_f = m_2 n \pi \Delta_{\text{int}}^2, \quad (14)$$

where $\Delta_{\text{int}} = R_0/\sqrt{\gamma}$ is the radius of the vortex core, and we have chosen to consider a vortex in component 1 filled by component 2. On the other hand, the effective mass of the vortex itself may be obtained by taking into account the relativistic character of the collective excitations of BEC coupled to the vortex state [43,44]:

$$m_v = E_v/c_s^2, \quad (15)$$

where $E_v = \pi n_1 \hbar^2 \ln(R_{\text{tot}}/\Delta_{\text{int}})/m_1$ is the energy of a vortex in BEC 1 in a cylindrical system limited by a container with a large radius R_{tot} , and $c_s = \sqrt{gn/m}$ is the sound speed in the trap center. Thus, the effective action, describing the degree of freedom of the system associated with the position of the vortex line element $\mathbf{R}(t)$, contains the “kinetic” contribution of the form

$$S_{\text{kin}} = \int dt (m_v + m_f) \dot{\mathbf{R}}^2/2. \quad (16)$$

The “potential” contribution describes forces acting on a vortex. It includes the Stern-Gerlach force applied to the filling composed of atoms of component 2 (in our system the force is directed along y),

$$S_{\text{ext}} = - \int dt \frac{m_f}{m_2} R_y \frac{\mu_B B'}{2}, \quad (17)$$

and the lift force, i.e., the quantum analog of the Magnus force, which may be derived from the GP model. In the derivation we start from the action for a two-component BEC,

$$S = \int dt \int d^3\mathbf{r} \left[\sum_{j=1,2} \text{Re}(i\hbar\psi_j^* \partial_t \psi_j) - \mathcal{E} \right]. \quad (18)$$

The potential contribution to the action associated with interaction of the vortex with the background velocity is

$$\begin{aligned} S_M &= \int dt d^2\mathbf{r} \text{Re}[i\psi_1^*(\mathbf{r} - \mathbf{R}(t)) \partial_t \psi_1(\mathbf{r} - \mathbf{R}(t))] \\ &= \frac{i}{2} \int dt d^2\mathbf{r} [\psi_1^*(\mathbf{r} - \mathbf{R}(t)) \nabla \psi_1(\mathbf{r} - \mathbf{R}(t)) \\ &\quad - \psi_1(\mathbf{r} - \mathbf{R}(t)) \nabla \psi_1^*(\mathbf{r} - \mathbf{R}(t))] \dot{\mathbf{R}}, \end{aligned} \quad (19)$$

where ψ_1 is the stationary wave function of a vortex (the chemical potential was dropped for brevity because it does not alter the result). The wave function $\psi_1(\mathbf{r} - \mathbf{R}(t))$ is Taylor expanded for small $\mathbf{R}(t)$ as

$$\psi_1(\mathbf{r} - \mathbf{R}(t)) = \psi_1(\mathbf{r}) + \mathbf{R}(t)\nabla\psi_1(\mathbf{r}) + O(\mathbf{R}^2, \dots), \quad (20)$$

and only the first order in $\mathbf{R}(t)$ is kept. After that the spatial integration is readily done, and we obtain, for a singly quantized vortex in component 1,

$$S_M = -v_1\pi\hbar n_1 \int dt \epsilon^{ij} R_i \dot{R}_j, \quad (21)$$

with $\epsilon^{12} = 1$, $\epsilon^{ij} = -\epsilon^{ji}$, $i, j = x, y$, and $v_1 = \pm 1$ is the winding number of the vortex with the effective vorticity along z (+1) or in the opposite direction (-1). It follows from the energetic conditions, and from our real-time numerical simulations, that vortices with $|v_1| > 1$ are not formed during the evolution of our system. Thus, vortices and antivortices experience opposite forces due to a background superfluid flow with velocity $\dot{\mathbf{R}}$. As a result, a single AT vortex in a homogenous two-component BEC is described in two dimensions by the action

$$S_v[\mathbf{R}, \dot{\mathbf{R}}] = S_{\text{ext}} + \int dt [(m_v + m_f)\dot{\mathbf{R}}^2/2 - v_1\pi\hbar n \epsilon^{ij} R_i \dot{R}_j]. \quad (22)$$

We note that the action of the external force on BEC 1 is not explicit in Eq. (22), because it implicitly contributes to $\dot{\mathbf{R}}$ by inducing collective bulk oscillations.

Equation (22) describes the quantum analog of the Magnus force, which acts perpendicularly to the velocity of a vortex $\dot{\mathbf{R}}(t)$. Using Eq. (22) and going to dimensionless variables specified in Sec. II, we obtain the dimensionless form of the force acting on a vortex in BEC 1 with nonsingular core filled by BEC 2:

$$\partial_{tt}^2 R_i = -\frac{4v_1\gamma R_0 \epsilon^{ij} \dot{R}_j + b_i(t)}{1 + 2\gamma \ln(\gamma R_{\text{tot}}/\xi_0)}, \quad (23)$$

where $b_i(t)$ are Cartesian components of the external force applied to BEC 2, $b_y(t) = b(t)$; see Eq. (3). Equation (23) shows that for systems with size $R_{\text{tot}} \lesssim (2/\sqrt{\gamma} R_0^2) \exp(1/2\gamma)$ the vortex mass is dominated by the mass of the core filling. In our system $R_{\text{tot}} \approx R_0$, and the vortex mass is approximately that of the filling. We conclude that the oscillations of the pair size observed in Fig. 11 are due to the bulk motion driven

by the external force and due to the external force applied to the filling. The motion of the bulk determines the bulk velocity with respect to vortices, and hence the Magnus force. As follows from Eq. (23), the frequency of the oscillations is close to the frequency of the external force, i.e., $\approx \Omega = 8.55$, which is confirmed by the numerical solution shown in Fig. 11.

V. SUMMARY

We have studied the parametric instability at the interface of two immiscible BEC components pushed towards each other by an oscillating force. The instability develops due to the parametric resonance, which pumps quantum capillary waves at the interface. At moderate amplitudes of the driving force the instability is stabilized at the nonlinear stage due to modifications of the doubled oscillation frequency in comparison with the frequency of the driving force. In that case the BEC interface demonstrates oscillations with modulated amplitude, which depends on the strength of the driving force. When the amplitude of the driving force is large enough, we observe detachment of droplets from BEC components and generation of quantum vortices—skyrmions. The skyrmions are born as vortex pairs and move almost stationarily from the interface to the trap edge. The properties and dynamics of the skyrmion pairs are discussed. We have introduced the critical velocity v_{cr} of a droplet of one BEC in a bulk of another BEC from topological arguments and derived the analytical formula for the quantum counterpart of the Magnus force acting on skyrmions.

Note added in the proof. Recently, the authors became aware of the work [45] on the Faraday resonance in two-component BEC confined to a quasi 1D geometry. The main difference between the current work and Ref. [45] is in the geometry (multidimensional versus 1D, respectively) and in the nature of the surface waves amplified by the oscillating external force. Here we study interfacial capillary modes on the common surface of two BECs, while in the work [45] these are the surface modes at the edges of each BEC facing vacuum.

ACKNOWLEDGMENTS

This research was supported partly by the Swedish Research Council (VR) and by the Kempe Foundation. Calculations have been conducted using the resources of High Performance Computing Center North (HPC2N). D.K. is grateful to Professor C. J. Pethick for inspiring discussions.

-
- [1] C. Becker *et al.*, *Nat. Phys.* **4**, 496 (2008).
 [2] C. Hamner, J. J. Chang, P. Engels, and M. A. Hoefer, *Phys. Rev. Lett.* **106**, 065302 (2011).
 [3] G. Nardin *et al.*, *Nat. Phys.* **7**, 635 (2011).
 [4] R. Blaauwgeers, V. B. Eltsov, G. Eska, A. P. Finne, R. P. Haley, M. Krusius, J. J. Ruohio, L. Skrbek, and G. E. Volovik, *Phys. Rev. Lett.* **89**, 155301 (2002).
 [5] H. Takeuchi, N. Suzuki, K. Kasamatsu, H. Saito, and M. Tsubota, *Phys. Rev. B* **81**, 094517 (2010).
 [6] N. Suzuki, H. Takeuchi, Kenichi Kasamatsu, M. Tsubota, and H. Saito, *Phys. Rev. A* **82**, 063604 (2010).
 [7] W. Wan, S. Jia, and J. Fleischer, *Nat. Phys.* **3**, 46 (2007).
 [8] M. A. Hoefer, M. J. Ablowitz, I. Coddington, E. A. Cornell, P. Engels, and V. Schweikhard, *Phys. Rev. A* **74**, 023623 (2006).
 [9] V. Bychkov, M. Modestov, and M. Marklund, *Phys. Plasmas* **15**, 032309 (2008).
 [10] M. A. Hoefer, J. J. Chang, C. Hamner, and P. Engels, *Phys. Rev. A* **84**, 041605 (2011).
 [11] D. Kobayakov, A. Bezett, E. Lundh, M. Marklund, and V. Bychkov, *Phys. Rev. A* **85**, 013630 (2012).
 [12] V. Bretin, S. Stock, Y. Seurin, and J. Dalibard, *Phys. Rev. Lett.* **92**, 050403 (2004).

- [13] K. Sasaki, N. Suzuki, and H. Saito, *Phys. Rev. Lett.* **104**, 150404 (2010).
- [14] M. F. Andersen, C. Ryu, P. Clade, V. Natarajan, A. Vaziri, K. Helmerson, and W. D. Phillips, *Phys. Rev. Lett.* **97**, 170406 (2006).
- [15] M. Mottonen, V. Pietila, and S. M. M. Virtanen, *Phys. Rev. Lett.* **99**, 250406 (2007).
- [16] B. P. Anderson, P. C. Haljan, C. A. Regal, D. L. Feder, L. A. Collins, C. W. Clark, and E. A. Cornell, *Phys. Rev. Lett.* **86**, 2926 (2001).
- [17] V. A. Mironov, A. I. Smirnov, and L. A. Smirnov, *J. Exp. Theor. Phys.* **112**, 46 (2011).
- [18] K. Sasaki, N. Suzuki, D. Akamatsu, and H. Saito, *Phys. Rev. A* **80**, 063611 (2009).
- [19] A. Bezett, V. Bychkov, E. Lundh, D. Kobayakov, and M. Marklund, *Phys. Rev. A* **82**, 043608 (2010).
- [20] D. Kobayakov, V. Bychkov, E. Lundh, A. Bezett, V. Akkerman, and M. Marklund, *Phys. Rev. A* **83**, 043623 (2011).
- [21] K. Sasaki, N. Suzuki, and H. Saito, *Phys. Rev. A* **83**, 053606 (2011).
- [22] J. S. Bai, J. H. Liu, T. Wang, L. Y. Zou, P. Li, and D. W. Tan, *Phys. Rev. E* **81**, 056302 (2010).
- [23] G. Dimonte and P. Ramaprabhu, *Phys. Fluids* **22**, 014104 (2010).
- [24] M. Hahn, D. Drikakis, D. Youngs, and R. Williams, *Phys. Fluids* **23**, 046101 (2011).
- [25] G. Dimonte and M. Schneider, *Phys. Rev. E* **54**, 3740 (1996).
- [26] S. Amiroudine, F. Zoueshtiagh, and R. Narayanan, *Phys. Rev. E* **85**, 016326 (2012).
- [27] R. Betti, R. L. McCrory, and C. P. Verdon, *Phys. Rev. Lett.* **71**, 3131 (1993).
- [28] S. Kawata, T. Sato, T. Teramoto, E. Bandah, Y. Masubishi, and I. Takahashi, *Laser Part. Beams* **11**, 757 (1993).
- [29] G. Searby, *Combust. Sci. Technol.* **81**, 221 (1992).
- [30] V. Bychkov, *Phys. Fluids* **11**, 3168 (1999).
- [31] V. Bychkov, A. Petchenko, V. Akkerman, and L.-E. Eriksson, *Phys. Rev. E* **72**, 046307 (2005).
- [32] V. Bychkov, D. Valiev, and L.-E. Eriksson, *Phys. Rev. Lett.* **101**, 164501 (2008).
- [33] A. Petchenko, V. Bychkov, V. Akkerman, and L.-E. Eriksson, *Phys. Rev. Lett.* **97**, 164501 (2006).
- [34] A. Petchenko, V. Bychkov, V. Akkerman, and L.-E. Eriksson, *Combust. Flame* **149**, 418 (2007).
- [35] C. J. Pethick and H. Smith, *Bose-Einstein Condensation in Dilute Gases*, 2nd ed. (Cambridge University Press, Cambridge, 2008).
- [36] I. E. Mazets, *Phys. Rev. A* **65**, 033618 (2002).
- [37] L. D. Landau and E. M. Lifshitz, *Mechanics* (Elsevier, Amsterdam, 2007).
- [38] T. H. R. Skyrme, *Proc. R. Soc. London A* **260**, 127 (1961).
- [39] Y. M. Cho, H. Khim, and P. Zhang, *Phys. Rev. A* **72**, 063603 (2005).
- [40] K. Kasamatsu, M. Tsubota, and M. Ueda, *Phys. Rev. A* **71**, 043611 (2005).
- [41] E. J. Mueller, *Phys. Rev. A* **69**, 033606 (2004).
- [42] K. Sasaki, N. Suzuki, and H. Saito, *Phys. Rev. A* **83**, 033602 (2011).
- [43] C. Wexler and D. J. Thouless, [arXiv:cond-mat/9612059v1](https://arxiv.org/abs/cond-mat/9612059v1).
- [44] G. E. Volovik, *Pis'ma Zh. Eksp. Teor. Fiz.* **65**, 201 (1997) [*JETP Lett.* **65**, 217 (1997)].
- [45] A. Balaz and A. I. Nicolin, *Phys. Rev. A* **85**, 023613 (2012).